



## OPEN Fabrication of an inorganic-organic hybrid based on lanthanum and trigonella grandiflora extract as an innovative corrosion inhibitor

Mahya Olfatmiri<sup>1</sup>, Mohammad-Bagher Gholivand<sup>1</sup>✉ & Mohammad Mahdavian<sup>2</sup>✉

This work presents a new and efficient biobased hybrid hinge based on lanthanum (La) cations and trigonella grandiflora (TG) extract, represented as La@TG, in a 3.5% NaCl solution, as an organic/inorganic mild steel corrosion inhibitor. The concentration of La cations and TG components released into the solution at various pH levels was assessed using UV-Vis/ICP-OES analysis. The composition and morphology of the adsorbed film were characterized using analytical techniques such as atomic force microscopy (AFM), Fourier-transform infrared spectroscopy (FTIR), energy-dispersive spectroscopy combined with scanning electron microscopy (SEM-EDS), and grazing incidence X-ray diffraction (GI-XRD) on the submerged electrode. Electrochemical techniques were leveraged to examine the effectiveness of the La@TG hybrid and to understand its inhibition mechanism in both solution and coating (intact and scratched) phases. The electrochemical analyses in the solution phase revealed that the La@TG hybrid exhibits relatively good corrosion resistance. Additionally, in the presence of an artificial flaw, the epoxy coating containing the La@TG hybrid showed strong active/barrier protection with self-healing qualities.

**Keywords** Biobased, Plant extract, Coating, Corrosion, Self-healing

Over the past century, surface protection for metals and alloys in corroding environments has attracted a lot of interest because of their growing use in industrial sectors like water purification, transportation, seafaring, and construction. One of the easiest and most affordable strategies to lower the alloys' corrosion rate in corrosive media is using organic or inorganic materials as corrosion inhibitors through chemisorption and physisorption. These materials can form barrier coatings that protect metal surfaces from corrosive chemicals. The actual issues with employing common corrosion inhibitors are related to their carcinogenic potential. Many studies have demonstrated the carcinogenic and toxic effects of substances such as hexavalent chromium. Consequently, scientists are searching for highly effective and non-toxic inhibitors of corrosion. In recent decades, it has been discovered that a variety of fragrant herbs and medicinal plants are valuable sources for use as organic anti-corrosion agents due to their affordability, high availability, eco-friendliness, and biodegradable properties<sup>1</sup>. It has been shown that these substitutes have better inhibition performance in acidic media than in neutral solutions<sup>2</sup>.

Although inorganic inhibitors tend to be more stable over time compared to organic inhibitors, some of them can be harmful to the environment and may not be biodegradable<sup>2,3</sup>. Using both organic and inorganic materials at the same time, corrosion inhibitors lead to a synergistic effect by forming chelates and insoluble complexes adsorbed on the immersed electrode surface<sup>4,5</sup>. Wang et al.<sup>6</sup> scrutinized the efficiency of inhibitive activity of a nanohybrid composed of rosemary extract and zinc chloride for AA5052 aluminum alloy in a solution of 0.05 M NaCl. Their findings demonstrated that the nanohybrid functioned as a mixed anodic and cathodic inhibitor, offering long-term anticorrosion protection because of the organic and inorganic components' synergistic interplay. Another organic/inorganic pair that Wamba-Tchio et al.<sup>7</sup> explored for lowering the corrosion rate of XC38 steel in a saline solution is the complex of zinc cations and extract from *Ficus pumila* linn. leaves. The obtained findings showed that the formation of insoluble precipitations between the organic substances and iron/zinc cations is responsible of the inhibition activity of the organic/inorganic hybrid.

<sup>1</sup>Department of Analytical Chemistry, Faculty of Chemistry, Razi University, Kermanshah, Iran. <sup>2</sup>Surface Coatings and Corrosion Department, Institute for Color Science and Technology, Tehran, Iran. ✉email: mbgholivand2013@gmail.com; mahdavian-m@icrc.ac.ir

In an independent investigation, Qian et al.<sup>8</sup> explored the effect of a hybrid composed of longan residue extract and sodium dodecylbenzene sulfonate on corrosion mitigation of a magnesium alloy in a NaCl medium. Their results demonstrated a synergistic impact between the constituents, emphasizing that the rates of anodic and cathodic corrosion reactions were lowered by the development of a compact coating on the alloy surface. Zhu et al.<sup>9</sup> demonstrated that cerium and glutamic acid (Glu) can function as a hybrid synergistic inhibitor for AA5052 in a saline electrolyte. The study found that this combination achieved a maximum inhibition efficiency of approximately 85% at concentrations of 0.05mM Glu + 0.30 Mm Ce<sup>3+</sup>. Sanaei et al.<sup>10</sup> examined the inhibition performance of a mixture of cichorium intybus leaf extract and zinc cations. Their study demonstrated that, in its hybrid form, this combination acted as a mixed-type inhibitor that shows good synergistic performance in mild steel (MS) electrodes in saline electrolytes. Ralkhah et al.<sup>11</sup> investigated Neodymium (III)-Benzimidazole as a hybrid anticorrosion agent. Their study demonstrated that the nanocomposite achieved maximal effectiveness of inhibition of approximately 83% for mild steel in a simulated seawater solution.

As far as we are aware, no article have been published on the combined benefits of corrosion inhibitive functioning achieved through the combination of plant extracts and lanthanum cations. Lanthanum cations (La<sup>3+</sup>) were specifically selected in this study due to the empty orbitals of La<sup>3+</sup> cations enable coordination with electron-donating functional groups present in plant extracts, thereby enhancing the stability and integrity of the hybrid organic–inorganic protective films formed on the metal surface. Nitrate salts were chosen as the lanthanum source due to the beneficial role of nitrate anions in corrosion inhibition. Nitrate ions can contribute to the overall electrochemical stability of the system and may exhibit synergistic effects in retarding corrosion, even when partially retained in the final precipitated product. For this reason, nitrate salts of transition and rare-earth metals are widely used in the development of hybrid corrosion inhibitors, as evidenced by numerous reports in the literature<sup>12,13</sup>. One type of organic coating known for its strong durability in both acidic and alkaline conditions, excellent adherence to steel, and high mechanical performance is epoxy coating (EPC)<sup>14,15</sup>. Despite these advantages, epoxy coatings have several drawbacks, such as poor long-term barrier performance, high brittleness, low impact resistance, and limited flexibility. These issues can result in the formation of cracks and pores during the curing process and in real-world applications<sup>16</sup>. Incorporating active and barrier fillers, as well as pigments, into coatings is a common method to enhance their mechanical and electrochemical performance<sup>17</sup>. The presence of active agents in organic coatings contributes to the emergence of intelligent coatings with self-healing properties<sup>18</sup>.

Throughout history, *Trigonella Grandiflora* (TG), a plant belonging to the papilionaceae family, has been harnessed for a variety of therapeutic motives<sup>19</sup>. In the pharmaceutical and medical literature of traditional Persian medicine, the TG pod or seedpod is referred to as *iklil-ul-malik*, milk vetch, European milkvetch, or *nakhonak*<sup>20</sup>. Many ailments, including dementia, vertigo, migraines, and strokes, have been treated with TG. However, there is no study on the anti-corrosion synergistic effects of the plant extract in the ubiquity of rare earth elements in saline-based solutions.

To prevent mild steel electrode corrosion, we tested the synergistic effects of mixing plant extract with lanthanum cations in a 3.5%wt. NaCl solution. The low carbon steel's surface was examined utilizing SEM, EDS, UV-Vis, FTIR, GI-XRD, and AFM measurements. The electrochemical characteristics of the corrosion inhibitors were assessed using polarization and electrochemical impedance spectroscopy (EIS) investigations.

## Experimental Materials

The TG samples were purchased from a local medicinal plant shop in Tehran. As stated by the plant shop, the TG, wild-grown in the southern region of Iran and collected in the spring, was used in this work. The TG has been assessed by the IUCN Red List (2010) and is currently listed as Least Concern<sup>21</sup>. Nitrate salt of La<sup>3+</sup> was purchased from Mojalali (Iran). The Khouzestan Petrochemical Company (Iran) provided the epoxy resin (Epiran 01, 75% solid). Polyaminopolyamide resin (Crayamid 115, 100% solid content) was obtained from Cray Valley and subsequently diluted with xylene to create a solution with a 50% solid content. Mild steel plates were provided by Foolad Mobarakeh. These plates were initially cleaned with acetone (Mojalali, Iran) and then polished with emery paper (Matador STARCKE, Germany) of varying grits from 220 to 1000 before use.

## Fabrication of organic-inorganic hybrid pigment

The choice between using extract powder and aqueous extract solution plays a significant role in the effectiveness and reliability of green corrosion inhibitors. Plant extract powders are generally more stable over extended periods, with minimal degradation of active constituents, especially under ambient storage conditions. For characterization techniques such as SEM–EDS (Bruker Nano, Germany), TG–DTG (Mettler Toledo TGA, USA), and XRD (PANalytical XPert PRO MPD, the Netherlands), testing can be directly performed on the powders without requiring further steps to remove moisture or separate phases. Therefore, we employed extract powder for handling and analysis and fabrication of extract solution.

To ensure high-quality SEM imaging and reliable elemental analysis by EDS, the samples were air-dried at room temperature and coated with a thin layer of gold using a sputter coater to enhance surface conductivity prior to imaging. SEM and EDS measurements were equipped with Esprit software and an XFlash 6|10 detector. The primary beam energy was set to 30 keV, with a take-off angle of 35°, azimuth angle of 45°, and a tilt angle of 0°. Data acquisition time was approximately 16.5 s. Further details, which may differ from sample to sample, are available in each image separately.

It should be mentioned that the extraction process concentrates bioactive compounds—such as alkaloids, flavonoids, tannins, and polyphenols which are known to play a pivotal role in corrosion inhibition. These compounds are typically present in small quantities in raw plant material, which predominantly consists of cellulose and other insoluble components. By converting these active molecules into a soluble form, extraction

facilitates more effective interaction with the metal surface and promotes the formation of a more uniform and adherent protective film. In contrast, the direct use of dried plant material may lead to lower inhibition performance due to poor solubility, undefined composition, and the presence of inactive or interfering substances. Therefore, the use of plant extracts represents a more efficient, reproducible, and scientifically sound approach for the development of green corrosion inhibitors.

In order to prepare the TG powder, dry leaves of *trigonella grandiflora* were first ground. To create the TG extract, 800 mL of distilled water and 55 g of TG powder were combined, and the mixture was agitated with a magnetic stirrer for 24 h at 70 °C. The electrolyte was then filtrated to remove the leaves and then dehydrated at 70 °C for 48 h. According to reports in the scientific literature<sup>22</sup>, the mixture was stirred for 24 h to ensure efficient release and extraction of bioactive compounds. This duration facilitates a more thorough extraction of phytochemicals from the plant material, thereby enhancing the quality and effectiveness of the extract as a corrosion inhibitor. The hybrid inhibitor was produced by combining lanthanum nitrate and TG extract in a 1:1 weight ratio. Specifically, 200 ml of deionized water were mixed with 0.2 g of lanthanum nitrate., followed by the addition of 0.2 g of the TG powder after complete dissolution. The mixture was agitated for 24 h. The resulting precipitate was subjected to four centrifugations (4000 rpm for 10 min) utilizing a centrifuge (RST16S, Iran) and washed with DI water. The precipitate was then desiccated for 48 h at 70 °C.

### Characterization of hybrid pigment

In this study, the synthesized hybrid pigment, referred to as La@TG, was characterized using FTIR, UV-Vis spectroscopy, and TG-DTA (thermogravimetry and differential thermal analysis) at a thermal ramp rate of 10 °C/min. FTIR spectroscopy was performed using Perkin-Elmer's Spectrum One (USA), covering a wavenumber span of 450–4000 cm<sup>-1</sup>. Formation of the complex between the precursors was examined using a UV-Vis spectrophotometer (Jenway 6715, United Kingdom).

To assess the stability of the synthesized hybrid at different pH levels (4, 7, and 11), ICP-OES (Inductively Coupled Plasma Optical Emission Spectroscopy, Agilent 730-ES) and UV-Vis measurements were performed. The pH of the solutions was adjusted using diluted HCl and NaOH solutions. Regarding this, 0.1 g of La@TG was dissolved in a saline solution and stirred for 24 h. After centrifugation, the supernatant was collected for subsequent analysis.

For 12 h at room temperature, the produced powder was stirred in a 3.5%wt. NaCl solution to create the corrosive electrolyte that contained the hybrid inhibitor. The electrochemical characteristics of bare steel plates (acting as the working electrode) immersed in electrolytes with and without the produced hybrid pigment were assessed using EIS and potentiodynamic polarization (PDP) studies, utilizing a three-electrode system. A beeswax-colophony mixture was used to electrically seal the mild steel coupons, leaving only a 1 cm<sup>2</sup> surface area exposed. The reference electrode was a saturated calomel electrode (SCE), while the counter electrode was platinum (Pt).

An AC signal with an amplitude of 10 mV was used for the EIS test at the open circuit potential (OCP) over a frequency range of 1 mHz to 100 kHz. The PDP test was performed using a DC span of ±250mV around the OCP. An IVIUM compactstat (the Netherlands) was utilized to collect the electrochemical raw data, and Zview software was used to match suitable equivalent electrical circuits to the EIS data.

### Analysis of the coating phase

Using a high-speed disperser, the La@TG pigment was blended into the epoxy resin and mixed well until the particle size was reduced to below 15 µm, measured using a grindometer. The hardener was then added to the epoxy component in a stoichiometric ratio. The resulting epoxy coating comprising 1 wt% of La@TG was denoted as EP/La@TG. In addition, inhibitor-free epoxy resin (Neat EP) was considered as the control sample. Mild steel plates, prepared as per Sect. Materials, were coated with the formulated mixtures. The obtained epoxy-based composites were then applied to the steel plates using a film applicator. The samples underwent a drying period of 10 days at 25 °C, followed by a baking phase lasting 30 min at 85 °C. A uniform thickness of approximately 70 ± 5 µm was achieved. Both intact and purposefully scratched samples were subjected to EIS following 35 days and 48 h, respectively, of subjection to a 3.5%NaCl electrolyte. A uniform area measuring 90 mm by 4 × 4 cm<sup>2</sup> with a specific film thickness was selected for analysis, while the remaining surface was protected using a method similar to that employed for samples in the solution phase.

To prepare the scratched coatings, a precise scratch of 0.5 cm in length was made with a sharp utility knife, reaching the metal substrate. After 10 days of immersion in a saline solution, the coatings were detached from the substrate, and SEM-EDS was used to evaluate the surface composition beneath the coating and in the scratched area.

To ensure the reproducibility of the data, duplicate samples were utilized for the electrochemical assessments. EIS analysis was performed on the control and La@TG-containing coatings in both intact and defective forms to assess the coating systems' ability to prevent corrosion. The EIS spectra were obtained using a method similar to that employed for samples in the solution phase.

## Results and discussion

### Characterization of La@TG

The FTIR spectrophotometer was leveraged to identify the functional groups in the TG extract and La@TG (Fig. 1a). The similarity of most peaks in both spectra indicates the presence of the same chemical bonds in the organic component of both samples. The presence of the La-O bond at 492 cm<sup>-1</sup> in the La@TG spectrum confirms the inclusion of the inorganic component in the hybrid sample. Strong peaks centered around 3440 cm<sup>-1</sup> indicate the existence of hydroxyl functions in these spectra. The bands observed at approximately 2930 cm<sup>-1</sup> correspond to the C-H bonds stretching vibration. In aromatic rings, the stretching vibration of C=C bonds

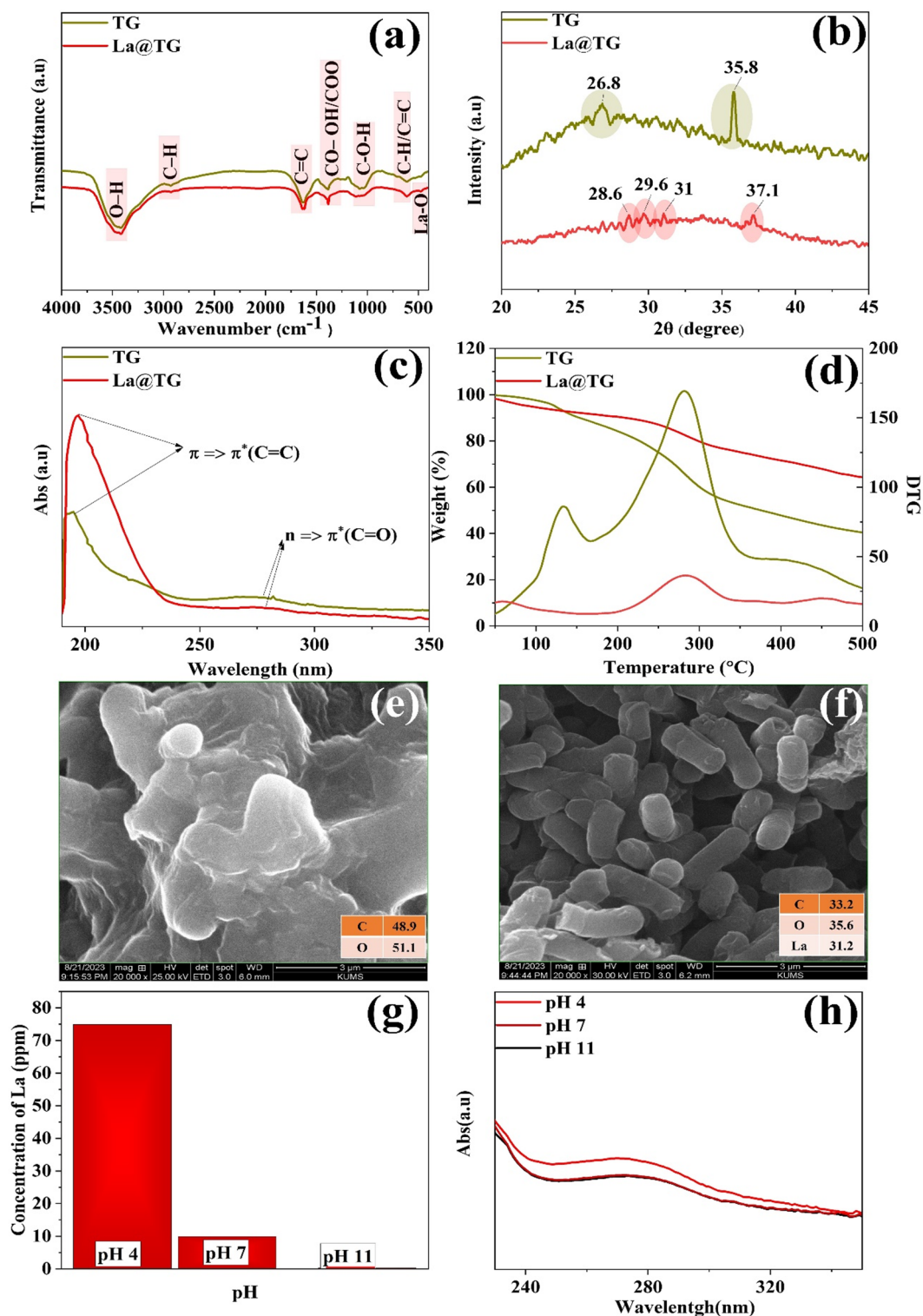


**Fig. 1.** (a) The powders of TG and La@TG analyzed using FTIR to obtain their spectra. (b) The XRD patterns of the powder derived from TG extract and the La@TG powder. (c) UV-Vis spectra of the TG extract in the absence and presence of lanthanum cations in a DI-based solution. (d) TGA and DTG data for TG and La@TG powders depicted in curves. (e, f) The SEM/EDS results of TG and La@TG powder. (g) Concentration of La cations released at various pHs. (h) The UV-Vis spectra of La@TG extract recorded at various pHs.



is linked to the absorption peaks at  $1625\text{ cm}^{-1}$ <sup>23,24</sup>. The peaks centered around  $1410\text{ cm}^{-1}$  are attributed to the stretching vibrations of COO and COOH bonds in the organic component. Both spectra exhibit peaks of C-OH stretching vibrations centered at approximately  $1076\text{ cm}^{-1}$ <sup>25</sup>. Additional absorption peaks in the  $400\text{--}1000\text{ cm}^{-1}$  wavenumber range might be connected to the C-H and C=C bonds' bending vibrations<sup>26</sup>.

The XRD test was conducted to examine the crystalline structure of the powder derived from the TG extract and the La@TG powder. The resulting diffraction patterns are shown in Fig. 1b. According to this figure, the diffraction pattern of the TG sample exhibits a broad peak in the angle range of  $20^\circ$  to  $35^\circ$ , which corresponds to the amorphous compounds present in the extract's structure. Additionally, the peaks located at  $26.8^\circ$  and  $35.8^\circ$  are attributed to the diffraction from the semi-crystalline structure of linoleic acid<sup>27</sup>. In the La@TG sample's XRD pattern, the peaks at  $28.6^\circ$ ,  $29.6^\circ$ ,  $31.0^\circ$ , and  $37.1^\circ$  can be related to the diffraction from the (110), (101), (200), and (201) planes of the  $\text{La}(\text{OH})_3$  structure (with JCPDS file PDF No. 36-1481), respectively<sup>28</sup>. The absence of the TG peaks in the XRD pattern of the organic-inorganic composite may be due to changes in the semi-crystalline structure of the substances exist in the TG extract in the presence of lanthanum cations.

To investigate the chemical bonds, present in the plant extract and interactions of the bonds with lanthanum cations, UV-Vis measurement was employed, and the resulting spectra are illustrated in Fig. 1c. In the spectrum of the extract without lanthanum, a peak and a shoulder are observable at wavelengths of 195 and 275 nm, respectively due to the electron transitions from the  $\pi$  to  $\pi^*$  antibonding orbitals of C=C bonds and from the  $n$  to  $\pi^*$  antibonding orbitals of C=O bonds<sup>29</sup>. In the lanthanum-containing sample, the same peak and shoulder are observed at wavelengths of 197 and 277 nm, but respectively with greater and lower intensities compared to the sample without lanthanum. This shift and intensity enhancement of the C=C band may be attributed to interactions between lanthanum cations and the carbon double bonds groups exist in the plant extract as was seen in other studies<sup>30</sup>. Additionally, the redshift and reduction in shoulder intensity in the presence of lanthanum could result from the lanthanum ions affecting the electronic structure of C=O bonds<sup>31</sup>. These findings revealed the occupancy of the C=C bond and carbonyl/carboxylic functions (C=O bond) in the plant extract compound, as well as the interaction of the bonds with the  $\text{La}^{3+}$  cations, confirming the hybrid structure of La@TG.

Thermogravimetric analysis (TGA) was used to assess the materials' thermal stability, and the resulting TGA and differential thermogravimetry (DTG) graphs are presented in Fig. 1d. The first weight loss stage occurs within the temperature range of 25 to 100 degrees Celsius and is linked to the desiccation of physically adsorbed water molecules on hydrophilic functional groups, such as carboxyl (COOH), hydroxyl (O-H), and carbonyl (C=O) groups. The subsequent weight loss stages occur in the temperature spans of 125–175 °C and 275–375 °C, which are associated with the degradation of aromatic structures and oxygen-containing ring structures, respectively. According to the TGA plot, the weight loss values of La@TG and TG extract were 40% and 63%, respectively, at 600 °C, indicating that the La@TG hybrid has more thermal stability than the TG extract. It can be due to the establishing coordination bonds between the organic and inorganic components.

SEM/EDS results of TG and La@TG powders are shown in Fig. 1e and f. The SEM micrograph of La@TG displays a crystal structure with a rod-shaped morphology. In contrast, the micrograph of TG shows an amorphous morphology. Furthermore, C and O elements' existence in the EDS results of both samples indicates that the elements are the basic components in the chemical structure of the samples. Furthermore, the occupancy of La element in the elemental composition of the La@TG samples proves that the chemical organic components in the TG extract had hybridized with  $\text{La}^{3+}$  cations in this sample.

Using the ICP-OES test, the releasing behavior of  $\text{La}^{3+}$  cations from the La@TG hybrid at different pHs was investigated (Fig. 1g). The higher  $\text{La}^{3+}$  cations releasing at lower pHs can be due to the protonation of the hybrid, leading to electrostatic repulsion forces between the positively charged organic molecules and the  $\text{La}^{3+}$  cations<sup>32</sup>. La ions, on the other hand, precipitate as oxide/hydroxide structures, causing the decrement of the  $\text{La}^{3+}$  cations concentration at higher pHs. Furthermore, the emancipation of the organic component from the hybrid pigment was assessed by UV-vis spectroscopy. The higher peak magnitude of the UV-Vis spectra of the La@TG-containing solutions at lower pHs (Fig. 1h) indicates that more concentrations of the TG component were released from the hybrid into the solution, which is in conformity with the ICP-OES results.

### Characterization of MS samples exposed to the La@TG solution

The FTIR spectra from the surface of electrodes submerged in the blank and La@TG-containing solutions are shown in Fig. 2a. In these spectra, the broad peak around  $3340\text{ cm}^{-1}$  correlates with the stretching vibration of O-H. For the TG-containing sample, the aliphatic C-H stretching mode appears as double absorption bands at 2930 and  $2884\text{ cm}^{-1}$ <sup>33</sup>. In addition, in this spectrum, the peaks of stretching modes of C=C,  $\text{CH}_2$ , C-H, and C-O bonds are located at 1614, 1469, 1367, and  $1034\text{ cm}^{-1}$ , respectively<sup>34,35</sup>. Furthermore, the peaks of stretching vibrations of the metal-oxygen (La-O) bonds were at 866, 630.4, and  $492.14\text{ cm}^{-1}$ <sup>36,37</sup>. The presence of the La-O stretching vibration peak in the La@TG hybrid sample indicates the emergence of a lanthanum oxide/hydroxide layer on the immersed electrode surface. The Fe-OH and Fe-O vibration peaks were observed at  $875\text{ cm}^{-1}$  and  $590\text{ cm}^{-1}$ , respectively. The existence of organic species on the MS surface submerged in the La@TG-containing solution is suggested by the identification of key functions in the TG extract, including linoleic acid. The increased intensity of the hydroxyl peak in the La@TG spectrum indicates that the hydroxyl groups have been chelated with  $\text{Fe}^{2+}$  and  $\text{La}^{3+}$  ions on the surface of MS. The decreased amount of corrosion-related substances on the submerged electrode's surface in the La@TG-containing medium is evidenced by the absence or low intensity of Fe-O and Fe-OH peaks in the La@TG sample's spectrum. These results show that an inhibitive layer has emerged on the surface of the electrode submerged in the electrolyte containing La@TG.

Grazing Incidence X-ray Diffraction (GI-XRD) is a surface-sensitive analytical technique used to study thin films and surface layers. Unlike conventional XRD, GI-XRD employs a very low incident angle, which limits the X-ray penetration depth and enhances the signal from the surface region<sup>38</sup>. This makes it particularly suitable for

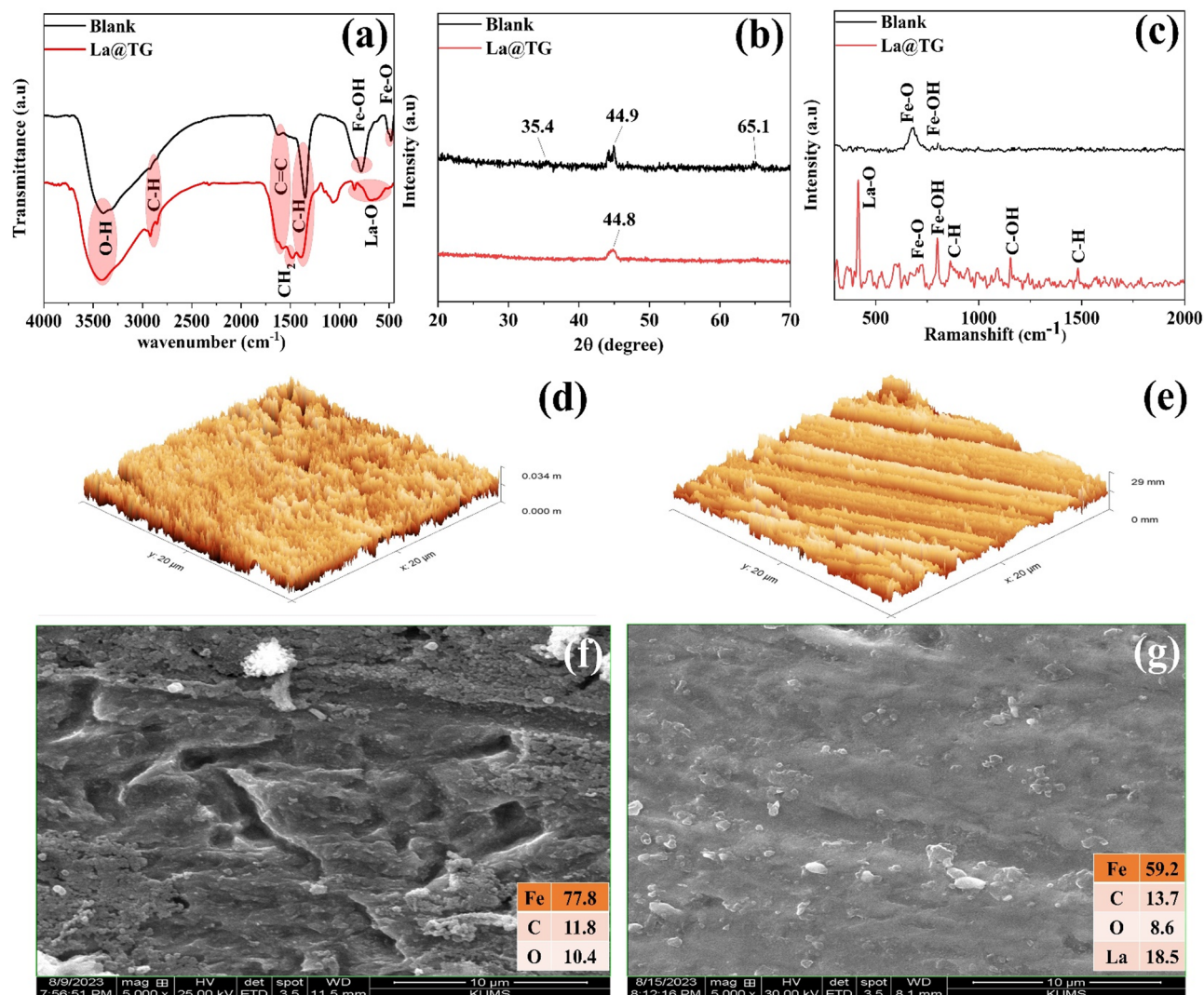


**Fig. 2.** (a) Steel sample FTIR spectra in the presence of Blank and La@TG solutions. (b) Raman spectra of the steel plates immersed in 3.5% NaCl solution with and without the La@TG. (c) GIXRD patterns of the steel coupons immersed in the saline solution without and with La@TG complex. (d, e) AFM micrographs of the mild steel sample without and with La@TG added, submerged in a 3.5% NaCl solution. (f, g) SEM/EDS of the mild steel sample without and with La@TG in a 3.5% NaCl solution.

characterizing the crystallographic structure, phase composition, and texture of thin coatings or adsorbed layers on substrates<sup>39</sup>. The crystalline layer that developed on steel that has been immersed in a saline solution was evaluated by GI-XRD analysis (Fig. 2b). When the specimen was dipped in the blank electrolyte, the diffraction pattern, three peaks are observed at 35.4°, 44.9°, and 65.1°, corresponding to the diffraction from the (311) and (400) planes of Fe(OH)<sub>3</sub> structure (according to JCPDS file PDF no. 65-3107)<sup>40,41</sup> and the (300) plane of Fe<sub>2</sub>O<sub>3</sub> structure (according to JCPDS file PDF no. 24-0072)<sup>42</sup>, respectively. These crystal structures attest to the development of oxide products on the MS's surface when submerged in saline. Contrarily, the diffraction pattern of the sample dipped in the saline electrolyte containing La@TG shows a decrease in the intensity of these peaks, with only the peak corresponding to the (311) plane of the Fe(OH)<sub>3</sub> structure at 44.8° being observable. This indicates a reduction in the corrosion products deposited on the surface, reflecting a decrease in the rates of anodic and cathodic corrosion reactions. The absence of peaks related to the inhibitive layer adsorbed on the surface in the X-ray diffraction pattern may be due to the very thin thickness of this layer (on the order of a few nanometers), which is below the detection sensitivity of the test.

To investigate the chemical bonds, present on the submerged steel plate surfaces in the corrosive environment, in both the corrosion inhibitor's presence and absence, Raman spectroscopy was performed and the resulting spectra are shown in Fig. 2c. In the spectrum of steel plate soaked in the blank environment, a strong peak at 669 cm<sup>-1</sup> and a weak peak at 790 cm<sup>-1</sup> are observed, corresponding to Fe-O and Fe-OH bonds present on the surface of the steel, respectively<sup>43</sup>. Upon adding the organic-inorganic inhibitor to the corrosive environment, new peaks emerge in the Raman spectrum, indicating the adsorption of various components of the inhibitor onto the surface of the steel. In this spectrum, the sharp peak at 415 cm<sup>-1</sup> is appropriate to the La-O stretching

vibration<sup>44,45</sup>, providing evidence for the adsorption of lanthanum cations as an oxide form on the surface of the steel. Additionally, the existence of C-H and C-OH bonds at 862, 1482, and 1154 cm<sup>-1</sup>, respectively<sup>46,47</sup>, confirms forming a layer of plant extract substances on the metal surface within the La@TG-containing corrosive environment. Furthermore, the decrease in the width and the Fe-O peak intensity may indicate a decreased degree of iron oxidation processes in the presence of the organic-inorganic inhibitor. Increase in intensity of the Fe-OH peak when exposed to this anti-corrosion agent could be attributed to complex formation between organic compounds and iron ions released from anodic regions. These complexes exhibit limited solubility in saline environments and strengthen the steel layer's defensive qualities.

The roughness and topology of the sodium chloride solution-soaked MS samples, both with and without the La@TG hybrid, were evaluated using AFM (Fig. 2d and e). The surface of the electrode dipped in the blank electrolyte has more corrosion products visible in the micrographs. For samples soaked in both the La@TG solution and the blank solution, average roughness values measured 30 nm and 108 nm, respectively. The development of a thick adsorbed layer on the steel surface, which slows down the pace of corrosion reactions, is responsible for the sample's decreased surface roughness while submerged in the treated solution. By acting as a hurdle and keeping aggressive species from getting to the electrode surface, this thick protective layer supports the results of electrochemical and SEM tests.

The MS specimens exposed to the blank and La@TG electrolytes were examined for surface morphology using SEM; the resulting micrographs are displayed in Fig. 2f and g, respectively. The existence of iron corrosion products on the blank specimen's surface, coupled with its high roughness, illustrates the significant extent of corrosion reactions that occurred when submerged in saline solution on the MS surface. In contrast, the smoothness observed on the MS surface treated with La@TG suggests a reduced rate of corrosion reactions. Furthermore, the quantity of corrosion products that developed on the MS surface was significantly reduced when this inhibitor was present. These results indicate that La@TG molecules can effectively diminish the corrosion rate of MS in saline environments.

Elemental analysis was conducted using a combination of EDS and surface mapping after submerging steel plates under various conditions. The elevated concentration of oxygen detected on bare steel soaked in saline solution confirms that iron oxide and hydroxide are present as corrosion products. In contrast, when La@TG was introduced, there was a significant reduction in Fe and O concentrations, suggesting that an organic/inorganic adsorbed film emerged on the MS surface. It is noteworthy that a high percentage of carbon detected in EDS results for samples containing La@TG corresponds to its carbon-rich structure. Additionally, detecting relatively high levels of lanthanum (La) on samples exposed to La@TG solution supports evidence for forming a protective film involving released La<sup>3+</sup> cations on the MS surface.

### Electrochemical measurements on samples exposed to the La@TG solution

To evaluate the synergistic inhibition performance between the inorganic (lanthanum cations) and organic (TG) inhibitors, EIS analysis was conducted, and the resulting spectra are presented as Bode plots in Fig. 3. According to Fig. 3, the Bode-impedance modulus plots for the blank sample indicate that the impedance at the lowest frequency did not show a specific trend relative to varying durations of immersion. This behavior can be linked to the emergence and detachment of porous corrosion products on the MS surface of the immersed electrode. In contrast, for the La@TG-containing sample, increase in parameter values with immersion duration from 3 to 48 h suggests progressive formation of an inhibitor layer on mild steel. Following this period, both the decrease in impedance value and phase angle (as the Bode-phase angle graphic illustrates) may result from defects forming within the inhibitive film on the electrode surface, leading to reduced corrosion resistance. The electrical equivalent circuits illustrated Fig. 3a and b were made use of to model the experimental EIS information. The resultant plots align closely with experimental curves presented in Fig. 3. It can be seen that the modeled data fit well with the experimental curves. The electrochemical parameters obtained are summarized in Table 1. In these electrical circuits,  $R_f$  denotes protective film resistance,  $R_{ct}$  indicates charge transfer resistance, and  $R_s$  represents solution resistance. The  $Q_{dl}$  and  $Q_f$  are the admittance of constant phase elements (CPE) connected to both formed films and double layers. The electrical circuits and related CPE parameters are reported in **Supporting Information (Table S1)**. The equivalent capacitance values of these constant phase elements were determined by using Eq. 1 and Eq. 2, respectively; results are provided in Table 1.

$$C_{dl} = (Q_{dl})^{(1/n)} \times \left[ \frac{R_{ct} \times R_s}{R_{ct} + R_s} \right]^{((1-n)/n)} \quad (1)$$

$$C_f = (Q_f)^{(1/n)} \times R_f^{((1-n)/n)} \quad (2)$$

In these equations, “n” is the exponent of the CPE, linked to the heterogeneity of the electrode. The blank sample's impedance plots display a time constant, suggesting that the corrosion reaction is controlled by charge transfer. The slight increase in  $R_{ct}$  values over the exposure period can be attributed to the formation of a surface oxide/hydroxide film on the metal, which offers semi-protective action<sup>48</sup>. The homogeneity and smoothness of the surface are reflected in the values of n. The uninhibited sample's declining trend in  $n_{dl}$  values suggests a coarser surface brought on by extended immersion periods or inhomogeneities brought on by the surface's accumulation of corrosion products<sup>49</sup>. It is crucial to remember that the production of porous corrosion products and the abundance of water molecules close to the surface are responsible for the blank sample's high  $C_{dl}$  values. Furthermore, the increasing trend in  $C_{dl}$  values for the uninhibited sample may outcome of the weak adhesion of corrosion products to the electrode surface, which can be easily separated from the substrate, leading to a reduction in capacitance thickness<sup>50</sup>.



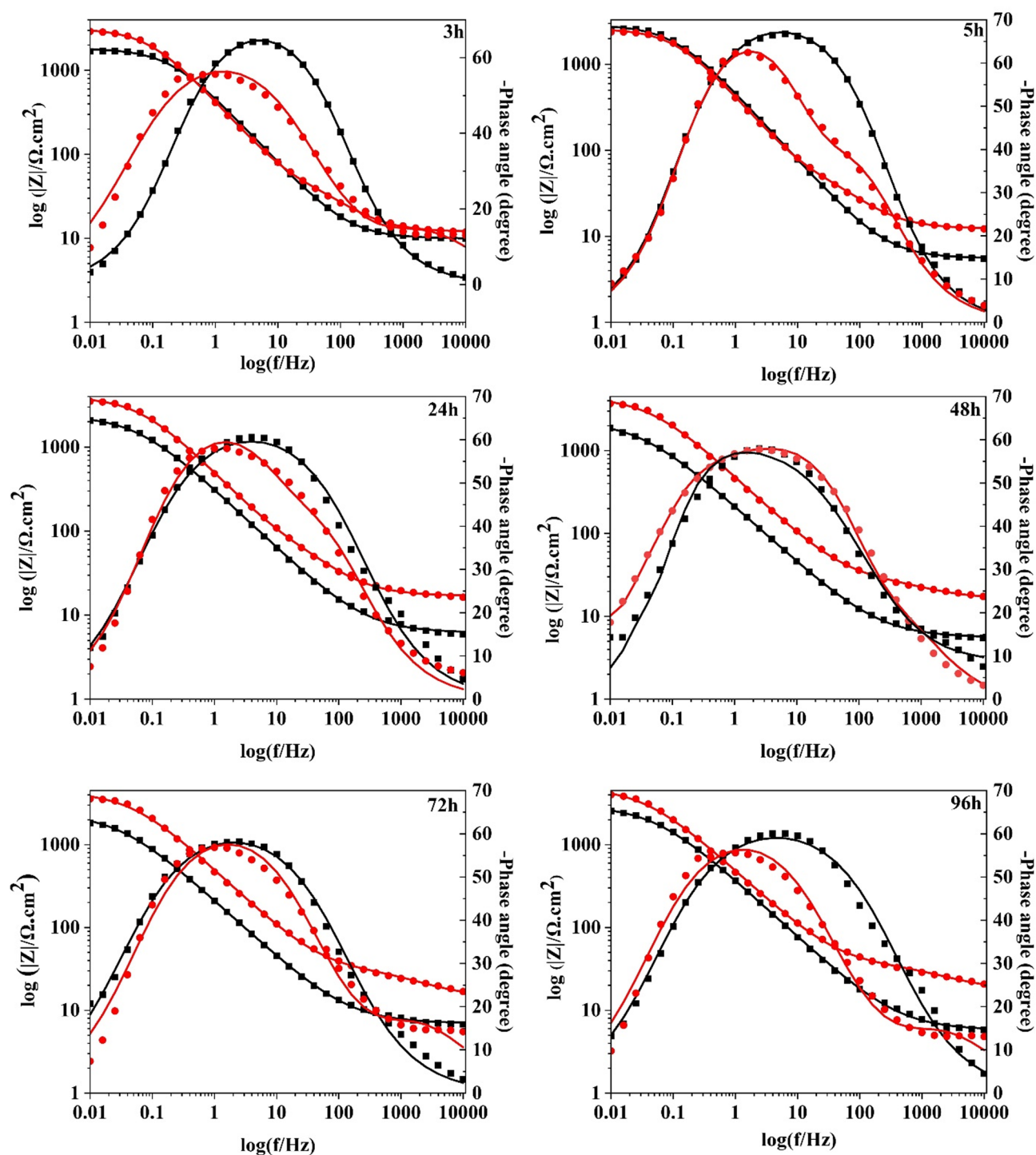


**Fig. 3.** Bode-impedance modulus and Bode-phase angle plots of the blank (■) and La@TG-containing (●) samples immersed for 3, 5, 24, 48, 72, and 96 h in the corrosive medium.

The Bode graphs at high frequencies show a distinct time constant in the sample containing La@TG, suggesting the development of an inhibitive layer on the exposed steel panels. Clearly the inhibited sample exhibits higher  $R_{ct}$  values all exposure times compared to the blank sample, confirming the effective corrosion protection of the steel provided by the hybrid organic-inorganic compound. It is noteworthy that the  $R_{ct}$  value of the La@TG-containing sample reached its maximum (5005  $\Omega \cdot \text{cm}^2$ ) after 96 h. As shown in Table 1, the  $C_{dl}$  values decrease due to the adsorption of the anti-corrosion agent, this causes the double-layer thickness to grow and/or the local dielectric constant to decrease<sup>51</sup>. The lowest  $C_{dl}$  value was observed after 48 h of exposure to steel in the inhibited solution, indicating that this sample contains a greater amount of inhibitor molecules adhered to its surface than other samples. The introduction of the organic/inorganic complex entering the



Sample	Time (h)	$R_s$ (ohm.cm <sup>2</sup> )	$R_f$ (Ohm.cm <sup>2</sup> )	$C_f$ (μF/cm <sup>2</sup> )	$C_{dl}$ (μF/cm <sup>2</sup> )	$R_{ct}$ (Ohm.cm <sup>2</sup> )
Blank	3	9.8 ± 0.56	–	–	104.6 ± 5.2	1822 ± 65.9
	5	5.5 ± 0.87	–	–	98.0 ± 1.9	1824 ± 65.9
	24	6.2 ± 0.77	–	–	141.1 ± 4.2	2421 ± 65.9
	48	5.9 ± 0.67	–	–	149.4 ± 9.0	2330 ± 76.9
	72	7.1 ± 0.45	–	–	190.1 ± 9.5	2449 ± 73.8
	96	6.3 ± 0.87	–	–	115.3 ± 5.8	3010 ± 28.7
La@TG	3	11.9 ± 1.1	62.5 ± 2.32	180.1 ± 31.0	89.7 ± 4.4	3029 ± 37.7
	5	12.3 ± 0.98	76.0 ± 3.32	104.7 ± 41.1	55.3 ± 2.7	2535 ± 38.9
	24	12.2 ± 1.3	71.7 ± 4.23	97.2 ± 25.7	86.0 ± 64.6	4071 ± 34.4
	48	16.3 ± 1.9	16.2 ± 2.12	14.1 ± 15.2	20.9 ± 0.83	4504 ± 45.8
	72	14.2 ± 2.2	19.5 ± 2.9	6.5 ± 14.7	45.5 ± 2.3	4411 ± 43.7
	96	17.4 ± 2.1	20.6 ± 3.3	5.5 ± 15.4	51.1 ± 2.5	5005 ± 54.8

**Table 1.** The obtained electrochemical parameters from the modeling of EIS data depicted in Fig. 3.

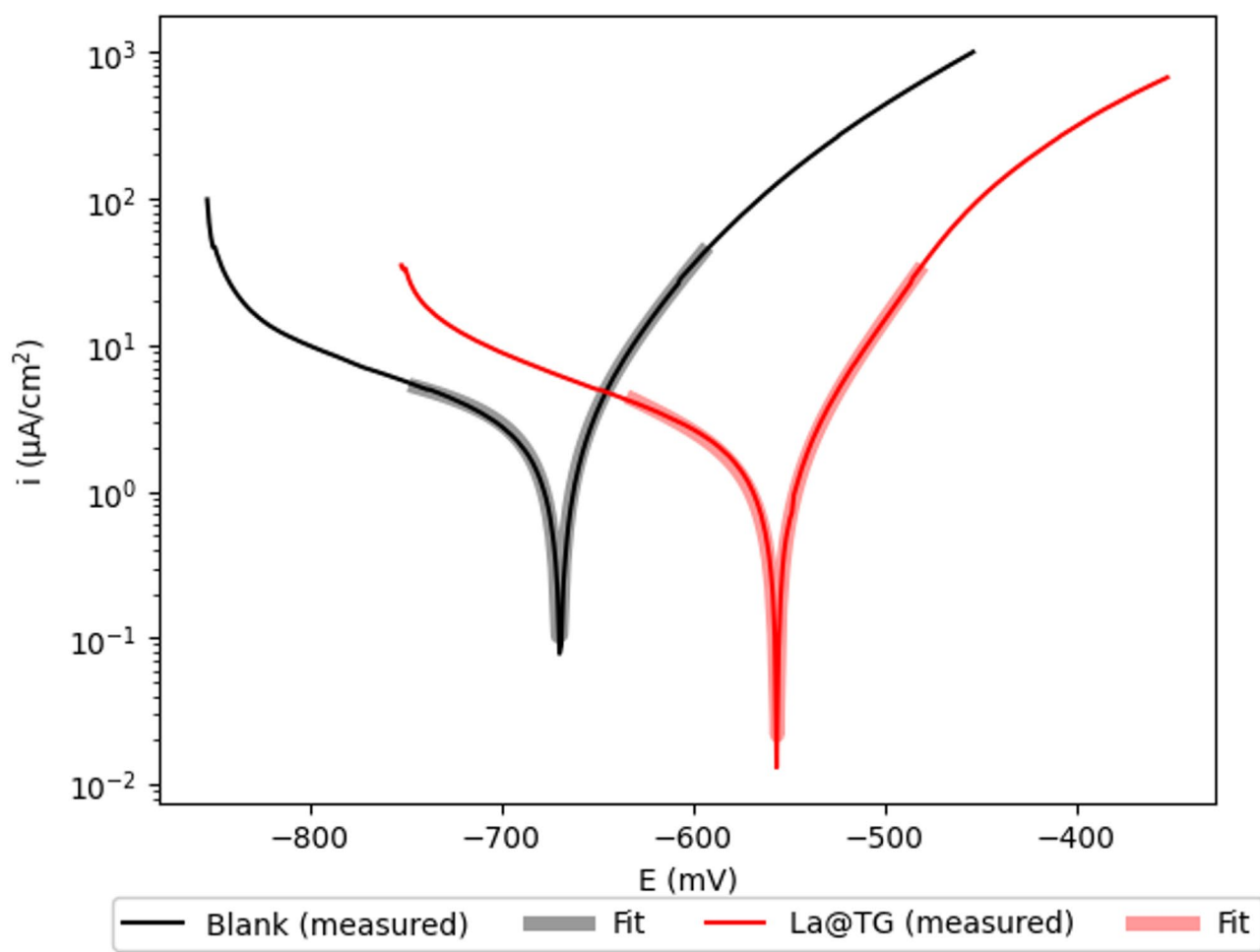


**Fig. 4.** Potentiodynamic polarization for immersed mild steel coupons in the blank and La@TG -containing solution.

corrosive electrolyte caused an increase in the  $R_f$  value during the initial immersion period, demonstrating an enhancement in the compactness or thickness of the inhibitive film. However, these values decreased over time due to the emergence of defects or local rust formation<sup>52</sup>.

The La@TG hybrid's anti-corrosion mechanism was further examined using the electrochemical polarization test (Fig. 4). The PDP graphs' examination reveals that the inhibitor's presence reduces the kinetics of both anodic and cathodic corrosion reactions, as seen by the curve's shift towards lower current densities. To

accurately determine the electrochemical parameters, the polarization curves were fitted with the Wagner-Traud equation (Eq. 3)<sup>53</sup>, and The fitting parameters for the polarization data, accomplished within  $\pm 75$  mV vs. OCP, are included in Table 2. This Table, the polarization resistance ( $R_p$ ) values were calculated using Eq. 4.

$$i = i_{corr} \left[ \exp \left( \frac{E - E_{corr}}{\beta_a} \right) - \left( \frac{E_{corr} - E}{\beta_c} \right) \right] \quad (3)$$

$$R_p = \frac{\beta_a \times \beta_c}{2.3031 \times i_{corr} \times (\beta_a + \beta_c)} \quad (4)$$

Here, the corrosion current density values of the blank and La@TG-containing samples are denoted by  $i_{corr}$ . Consequently, The density of corrosion current dropped from  $3.3 \mu\text{A}/\text{cm}^2$  to  $1.6 \mu\text{A}/\text{cm}^2$  in the presence of La@TG, indicating a reduction in the corrosion rate attributed to this hybrid compound. The approximately 52% increase in polarization resistance in contrast to the blank sample when the inhibitor is present provides further evidence of the La@TG effectiveness in improving the system's electrochemical properties. Additionally, Table 2 indicates that the potential for corrosion rose from  $-669.8\text{mV}$  to  $-556.3\text{mV}$  in the presence of the inhibitor, suggesting that La@TG can be classified as an anodic inhibitor. In other words, La@TG more effectively reduces the rate of anodic corrosion reactions.

Figure 4.

## Corrosion studies on coated samples

### Scratched coatings

EIS was used to examine the self-healing capabilities of the coating containing the La@TG hybrid pigment; the resulting Bode plots are shown in Fig. 5. An electrical equivalent circuit featuring two-time constants, which represent the double layer and coating, was chosen to model the electrochemical behavior of the systems.

The electrochemical parameters, including the capacitance of the solution resistance,  $R_s$ , double layer  $C_{dl}$ , charge transfer resistance of the double layer,  $R_{ct}$ , resistance of the film formed within the scratch,  $R_f$ , and capacitance of the coating film on the metal surface,  $C_f$ , were evaluated. The fitting results are presented in Table 3. Table S2 (**Supporting Information**) presents the values of  $Q_f$  and  $Q_{dl}$  values. At every immersion time, as illustrated in Fig. 5, the impedance at the lowest frequency for the coating using the anti-corrosion agent is higher than that for the blank coating, indicating improved corrosion resistance when La@TG is present. This enhancement can be attributed to species released from La@TG particles embedded in the coating that migrate into the scratched zones, forming a protective film over the defect areas<sup>54</sup>. Considering the fitted outcomes shown in Table 3 the coatings containing La@TG exhibited higher  $R_{ct}$  and  $R_f$  values at all immersion times compared to the blank sample. This increase is attributed to the leaching of active agents either beneath the coating or in the defective areas. It is widely recognized that coating delamination can be inferred from fluctuations in  $R_{ct}$  and  $C_{dl}$  values (Table 3)<sup>54</sup>. The decrease in  $R_{ct}$  and the increase in  $C_{dl}$  for the blank sample at longer immersion times indicate the progression of detachment and the emergence of corrosion products underneath the blank coating. In contrast, the existence of organic/inorganic active ingredients in the La@TG-containing coatings effectively delays the rate of coating delamination. As a result,  $R_{ct}$  values notably increased while  $C_{dl}$  values decreased across all immersion times. Specifically,  $C_{dl}$  values for both the blank and La@TG-containing coatings changed from  $385.5$  to  $771.7 \mu\text{F}/\text{cm}^2$  and from  $631.9$  to  $2.6 \mu\text{F}/\text{cm}^2$ , respectively, with increasing immersion time. The higher  $R_{ct}$  values and lower  $C_{dl}$  values observed for the coating loaded with La@TG, compared to the blank coating at longer immersion times, are likely due to the formation of an adsorptive inhibitor film on the surface of the steel panel. This film contributes to a fragmentary recovery of the coating's blockade properties. As shown in Table 3 the resistance of the coating ( $R_f$ ) was enhanced by incorporating anti-corrosion molecules into its structure. The  $R_f$  values for the blank and La@TG coatings after 3 h of immersion were measured at  $565 \Omega \cdot \text{cm}^2$  and  $10,151 \Omega \cdot \text{cm}^2$ , respectively. The higher  $R_f$  value of the composite coating compared to the neat coating may be attributed to the enhanced active/barrier performance of the La@TG coating. After 96 h, the estimated  $R_f$  values for the coatings without and with the anti-corrosion agent were  $251 \Omega \cdot \text{cm}^2$  and  $20,411 \Omega \cdot \text{cm}^2$ , respectively. The greater  $R_f$  value for the composite coating after extended immersion indicates the long-term protective performance of the anti-corrosion agent used in the defective epoxy coating. In general, the variation of  $R_f$  with the immersion time can be considered an indicator of the resistance of a coating in an aggressive medium, and  $C_f$  can be utilized to study the water absorption of a coating<sup>55</sup>. From Table 3, it is evident that the  $R_f$  value for the La@TG coating increases with immersion time, reaching up to 48 h. This indicates that the leached inhibitor from the coating enhances the anti-corrosion performance of the affected coating. Additionally, Table 3 shows that the  $C_f$  values for the La@TG coating are significantly lower than those of the blank specimen across all dipping times, demonstrating superior active inhibitive capabilities of the treated coating at the artificially defected area.

Sample	$-\beta_c$ (mV/dec)	$\beta_a$ (mV/dec)	$E_{corr}$ (mV)	$i_{corr}$ ( $\mu\text{A}/\text{cm}^2$ )	$R_p$ ( $\Omega \cdot \text{cm}^2$ )
Blank	$151.8 \pm 7.6$	$28.7 \pm 1.4$	$-669.8 \pm 33.4$	$3.3 \pm 0.2$	3170.7
La@TG	$74.1 \pm 3.7$	$24.5 \pm 1.2$	$-556.3 \pm 27.8$	$1.6 \pm 0.08$	5085.5

**Table 2.** Potentiodynamic polarization characteristics related to mild steel tests immersed in 3.5% NaCl solution, either with or without La@TG extract, for 96 h.

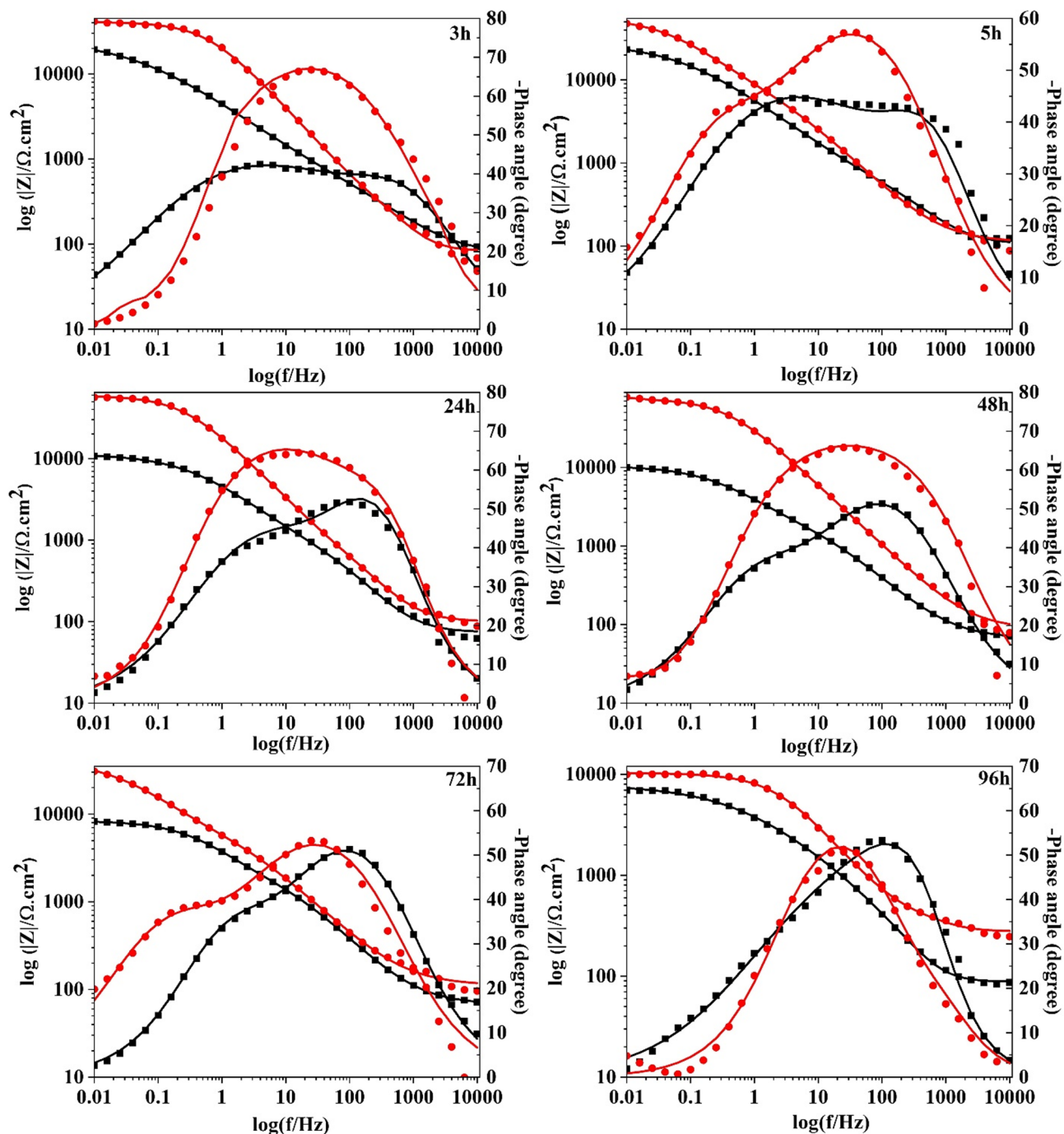


**Fig. 5.** Bode-impedance modulus, and Bode-phase angle plots of the blank (■) and La@TG -containing (●) scratched coatings immersed for 3, 5, 24, 48, 72, and 96 h in the corrosive medium.

The releasing of the La@TG organic-inorganic complex from the artificially defected coating and the formation of a passive film in the scratch area can be identified using SEM and EDS analyses in the scratched region (Fig. 6). In the scratched area of the blank coating, corrosion products are clearly visible. Their presence is confirmed by the EDS spectrum, which indicates significant atomic and weight percentages of iron and oxygen. In the case of the La@TG-coated sample, notable concentrations of carbon and lanthanum confirm the formation of a thin film of adsorbed inhibitors in the defect zone. The findings of the electrochemical tests show that this inhibitive film greatly improves the scratched coating's resistance to corrosion.

#### Intact coatings

Barrier/active inhibition of intact coatings was investigated using the EIS test, and the Bode plots are shown in Fig. 7. Two equivalent circuits, one with a single time constant and the other with two-time constants, were

Sample	Time	$R_s$	$R_f$ (Ohm.cm <sup>2</sup> )	$R_{ct}$ (Ohm.cm <sup>2</sup> )	$C_f$ (μF/cm <sup>2</sup> )	$C_{dl}$ (nF/cm <sup>2</sup> )
	(h)	(Ohm.cm <sup>2</sup> )				
Blank	3	75.9 ± 4.3	575.3 ± 13.2	24,298 ± 322.1	2.3 ± 0.3	385.5 ± 20.2
	5	99.8 ± 4.8	565 ± 11.2	2309 ± 432.9	6.0 ± 0.1	1023.7 ± 2.2
	24	79.0 ± 3.7	919.2 ± 21.2	10,554 ± 1232.3	10.3 ± 0.2	1432.6 ± 1.4
	48	68.9 ± 4.2	228.5 ± 44.3	8234.5 ± 298.3	9.7 ± 0.3	1362.4 ± 1.9
	72	65.7 ± 5.2	221.8 ± 32.8	6111.1 ± 321.2	9.6 ± 0.7	660.1 ± 5.1
	96	87.8 ± 5.1	251 ± 13.9	7498.2 ± 232.1	1.3 ± 0.2	771.7 ± 6.0
La@TG	3	84.3 ± 4.5	378.4 ± 13.4	40864.8 ± 109.6	0.6 ± 0.1	631.9 ± 1.2
	5	99.6 ± 3.2	10151.8 ± 98.7	46972.9 ± 112.8	2.3 ± 0.7	1.1 ± 0.06
	24	100.6 ± 6.1	1253.4 ± 120.8	58,563 ± 87.9	2.2 ± 0.4	457.6 ± 4.9
	48	88.03 ± 3.3	75289.9 ± 138.6	10762.8 ± 76.7	5.4 ± 0.3	268.2 ± 0.1
	72	110.5 ± 2.9	7483 ± 177.9	33412.7 ± 29.7	0.2 ± 0.1	3.6 ± 0.4
	96	279.4 ± 4.8	20,411 ± 123.7	9855 ± 11.9	0.9 ± 0.01	2.6 ± 0.01

**Table 3.** Electrochemical parameters extracted from EIS analysis for the blank and La@TG-containing scratched coatings at different immersion durations.

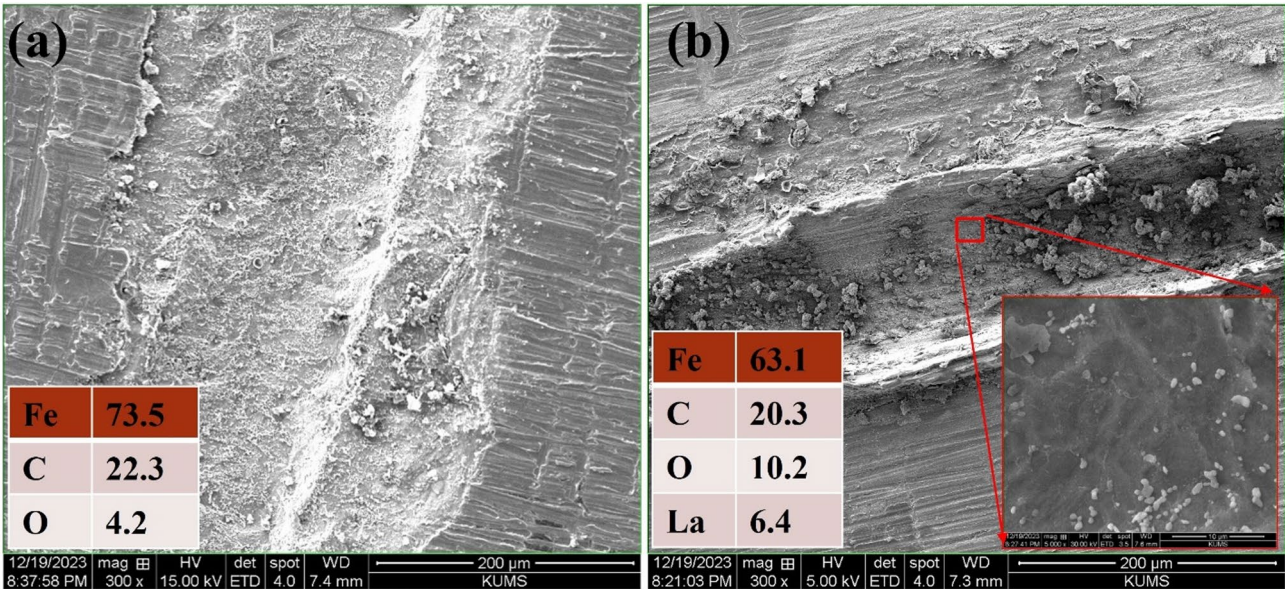


**Fig. 6.** SEM and EDS results from the scratched region of the defected coating containing **a** blank **b** La@TG inhibitor.

used to fit the impedance measurement data, with the obtained electrochemical parameters listed in Table 4. The extent of  $Q_f$  and  $Q_{dl}$  are reported in Table S3 (**Supporting Information**). In the corresponding circuits,  $R_{ct}$  stands for the charge transfer resistance,  $R_f$  is the coating resistance, and  $R_s$  represents the solution resistance. Besides,  $C_f$  and  $C_{dl}$  refer to the constant phase elements of the coating and the double layer, respectively. The total corrosion resistance of the systems under study can be determined by the low-frequency impedance<sup>56</sup>. In the absence of the anticorrosion active agent, the impedance modulus at the low frequency in Bode plots is reduced by passing time. In addition, the low capacitive conduct of the blank coating and the existence of the second time constant in the obtained plots during 28 d to 42 d of immersion in the aggressive medium indicates the corrosion process and the diffusion of electrolyte into the coating-MS contact. This can be due to the existence of open pores in the coating, leading to further decline of the blank coating barrier properties<sup>57</sup>. It is worth mentioning that the decrement in the high phase angle values at high frequencies in the Bode-phase angle plots at all soaking times proves a considerable reduction in the coating barrier efficiency<sup>58</sup>. Hydroxyl ions formed on the cathodic sites as a result of electrolyte penetration underneath the coating, which can increase pH at the coating/metal contact and impair adhesion connections<sup>59</sup>. However, the La@TG-coating sample's impedance values at the lowest frequency are greater than those of the blank. coating during the whole exposure time. Also, the phase angle at all immersion times is close to  $-90^\circ$ , revealing the appropriate barrier functioning of the La@TG coating. It should be noted that the extent of breakpoint frequency (a frequency with a  $-45^\circ$  phase angle) for the La@TG coating is much lower than that for the blank coating, which reflects a decline of microscopic



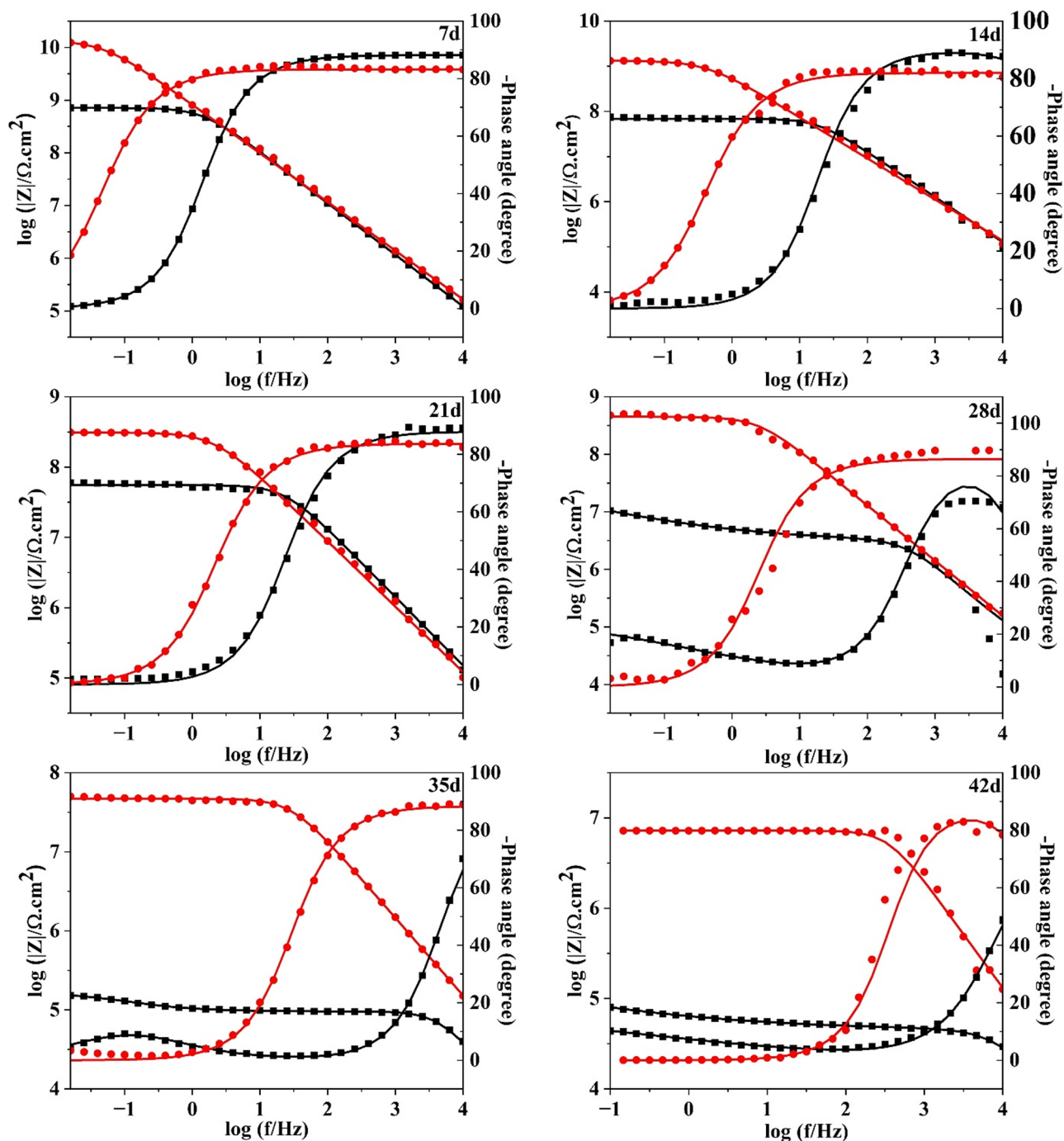


**Fig. 7.** Bode-log  $|Z|$  and Bode-phase angle plots of the blank (■) and La@TG -containing (●) samples at various soaking durations (markers and solid lines are the experimental and fitted data, respectively).

delamination sites in the presence of the anticorrosion agent<sup>60</sup>. The inhibition performance comes from the penetration of the active agents in the coating along with the electrolyte to the coating-steel interface, resulting in diminish in the corrosion rate. The values of equivalent capacitance of the constant phase elements are computed using Eq. 1 and Eq. 2<sup>61</sup>.

It was observed in Table 1 that the degree of resistance to coatings when there is the organic/inorganic agent was improved at all immersion times, manifesting a prominent barrier characteristic of the La@TG coating. After 7 days of immersion, the  $R_f$  value for the neat and La@TG coating was estimated to be 709 MOhm.cm<sup>2</sup> and 13,610 MOhm.cm<sup>2</sup>, respectively. In fact, for the La@TG coating,  $R_f$  values increased owing to the barrier properties of this sample. From Table 4 for the La@TG sample, the higher  $R_f$  value after 28 days of immersion (311 MOhm.cm<sup>2</sup>) than that obtained for the sample immersed for 21 days (309 MOhm.cm<sup>2</sup>) can be due to pore plugging of the coatings with the reaction of corrosion products and inhibitors leached from La@TG or active

Sample	Immersion time (days)	Equivalent circuits	$R_f$ (Mohm.cm <sup>2</sup> )	$C_f$ (nF/cm <sup>2</sup> )	$R_{ct}$ (Mohm.cm <sup>2</sup> )	$C_{dl}$ (nF/cm <sup>2</sup> )
Blank	7	R(QR)	709.6 ± 11.7	0.18 ± 0.02	–	–
	14	R(QR)	70.4 ± 3.1	0.16 ± 0.01	–	–
	21	R(QR)	53.9 ± 0.6	0.21 ± 0.02	–	–
	28	R(Q(R(QR)))	2.9 ± 0.1	0.23 ± 0.02	699.8 ± 11.3	0.07 ± 0.01
	35	R(Q(R(QR)))	0.08 ± 0.01	0.28 ± 0.03	6954 ± 119.7	1.2 ± 0.1
	42	R(Q(R(QR)))	0.04 ± 0.01	0.35 ± 0.03	5012 ± 111.9	1.6 ± 0.1
La@TG	7	R(QR)	13,610 ± 1123	0.19 ± 0.02	–	–
	14	R(QR)	1335 ± 102	0.21 ± 0.02	–	–
	21	R(QR)	309 ± 17.8	0.30 ± 0.03	–	–
	28	R(QR)	311 ± 12.7	0.15 ± 0.01	–	–
	35	R(QR)	46.8 ± 6.7	0.43 ± 0.04	–	–
	42	R(QR)	7.2 ± 0.6	0.71 ± 0.06	–	–

**Table 4.** Electrochemical parameters of the intact blank and La@TG-containing epoxy samples.

Sample	$\dot{E}$ (MPa)	$T_g$ (°C)	$T_R$ (K)	$v_e$ (mol/m <sup>3</sup> )	$\tan \delta$
Neat EP	940.7	77.3	375.3	0.1	0.39
EP/La@TG	1990.6	93.5	391.2	0.2	0.57

**Table 5.** Results from the DMTA test for the neat EP and EP/La@TG coating samples.

inhibition of the La@TG at the Fe-coating interface leading to higher performance of the system<sup>54,62</sup>. After 42 days of immersion, this value for the blank and La@TG coating was about 7 kOhm.cm<sup>2</sup> and 7200 kOhm.cm<sup>2</sup>, respectively, which is related to the presence of the anti-corrosion agent in the coating matrix, causing higher resistance against the corrosive ions. The increase in the  $C_f$  by adding corrosion inhibitors into the coating, especially at longer dipping times, can be linked to the partial dissolution of La@TG, leaving the coating matrix partially filled with water molecules. The value of  $C_f$  for the neat and La@TG coating after 42 days of soaking in the saline media was about 0.35 nF/cm<sup>2</sup> and 0.71 nF/cm<sup>2</sup>, respectively. Such differences in the  $C_f$  values can be linked to the leaching of the La@TG moieties from the coating.

**Mechanical studies of coatings and coated samples**

Dynamic Mechanical Thermal Analysis (DMTA) is a technique used to evaluate the viscoelastic behavior of polymeric materials as a function of temperature, time, or frequency<sup>63</sup>. In this test, a small oscillatory force is applied to the sample, and the material’s response is measured in terms of storage modulus (representing elastic behavior), loss modulus (representing viscous behavior), and the damping factor ( $\tan \delta$ ), which is the ratio of the two. DMTA is particularly useful for determining the glass transition temperature ( $T_g$ ) and energy dissipation characteristics of materials<sup>64</sup>. In our study, DMTA was performed on neat epoxy and epoxy containing the La@TG hybrid to assess the influence of the hybrid filler on the thermal and mechanical properties of the epoxy matrix. This test helps reveal how the incorporation of La@TG affects the  $T_g$  and damping behavior of the composite, which are critical for evaluating its performance under mechanical and thermal stress. The addition of La@TG to epoxy coatings may cause positive or negative effects on the curing (cross-linking) process, as well as mechanical and thermal characteristics. The DMTA was carried out to elucidate these effects, and the outcomes that were attained are represented in Table 5 and Fig. 8a. From the DMTA data, the variations in the  $\tan \delta$  (loss factor) and storage ( $E'$ ) and loss ( $E''$ ) modules as an operation of the predetermined temperature range ( $T = 25\text{--}125^\circ\text{C}$ ) were retrieved. The ratio of  $E''$  to  $E'$  is described by the loss factor. Equation 5 was utilized to calculate the cross-linking density ( $v_e$ ) using the data ( $E'_r$  and  $T_r$ ) derived from the gas constant and the rubbery plateau area ( $R = 8.314 \text{ J.mol}^{-1}\text{K}^{-1}$ ).

$$v_e = \frac{\dot{E}_r}{3RT_r} \tag{5}$$

The polymer’s elastic deformation,  $E'$ , indicates the cross-linking statistics<sup>65</sup>. The graphs suggest that the La@TG/EPC and EPC samples’  $E'$  value gradually and continuously decreases with temperature, indicating that greater temperatures cause the epoxy molecular chains to weaken<sup>66</sup>. The mobility of free polymer segments improves with temperature, and the energy stored is transformed into heat. This causes the glassy-to-rubbery transition of epoxy, which is a dramatic drop in the material’s modulus within a particular temperature range. The glass-transition temperature ( $T_g$ ) commonly describes the temperature range corresponding reaching the loss factor’s highest values (height). Rapid mechanical strength degradation occurs in this transition area. At temperatures above  $T_g$ , the polymer exhibits viscoelastic behavior, and the molecular segments are free to slide and move<sup>44</sup>.  $E'$ , loss factor, cross-linking density, and  $T_g$  were around 940.7 MPa (25 °C), 0.39, 0.1 mol/cm<sup>3</sup>, and 77.3 °C for the pure epoxy coating (EPC), respectively. The presence of the La@TG particles caused to change the  $E'$ ,  $T_g$ , and

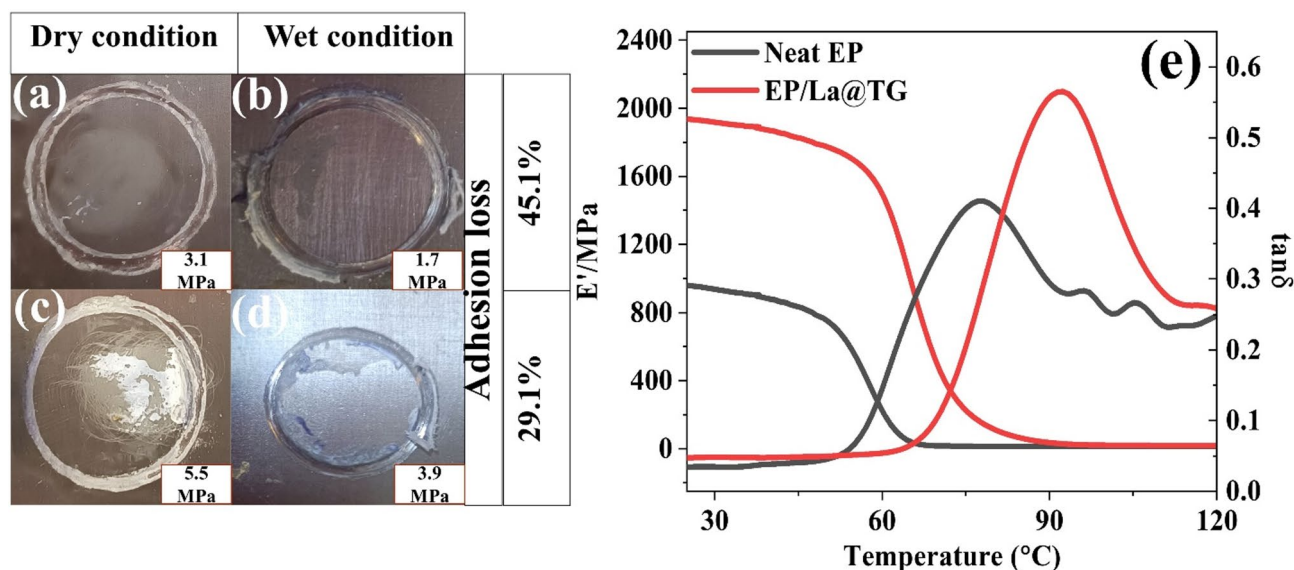


**Fig. 8.** Pull off results for (a, b) EP, (c, d), EP/La@TG wet and dry adhesion; (e) DMTA examination of the neat EP and EP/La@TG samples.

cross-linking density values to 1990.6 MPa, 0.2 mol/cm<sup>3</sup>, and 93.5 °C, respectively. The cardinal cause for the improvement of the thermal-mechanical features of the nanocomposite is the fact that the uniform dispersion of the hybrid particles in the epoxy-based composite helps in distributing stress more evenly. In addition, the inorganic component (lanthanum) can provide reinforcement to the polymer matrix<sup>67</sup>, while the organic compounds can offer flexibility and toughness<sup>68</sup>. This synergistic effect can result in a coating with superior thermal-mechanical properties. The above-mentioned mechanism caused to the higher crosslinking density, and so, more transition temperature of the composite coating compared to the pure epoxy-based coating.

The adhesion capability of the coatings was assessed using the pull-off technique both while they were dry and after 14 days of exposure to a salt spray chamber. The adhesion strength and pictures of the specimens following the dollies' removal are shown in Fig. 8. The findings indicate that the inclusion of the La@TG hybrid led to an increase in the adhesion strength of the coating. The calculation of adhesion loss (AL) in coatings was performed utilizing Eq. 6, where  $\Gamma_d$  refers to the adhesion in dry conditions and  $\Gamma_w$  denotes the adhesion in wet conditions.

$$AL = \frac{\Gamma_d - \Gamma_w}{\Gamma_d} \times 100 \quad (6)$$

Van der Waals interactions, including hydrogen bonds, can be produced by the interaction of La-based oxide/hydroxide compounds with polar oxygen-containing functional groups, such as carbonyl and hydroxyl groups. Additionally, the La-oxide film's active hydrogen can form solid chemical connections with the polymer matrix. The coating may separate from the underlying metal surface as an outcome of the emergence of corrosion products underneath it. The presence of La@TG dramatically lowers coating delamination by reducing corrosion processes at the coating-metal substrate contact. These mechanisms may contribute to enhanced wet adhesion and decrease the AL value<sup>69</sup>.

## Conclusion

This study explored the inhibition performance of La@TG for mild steel in a saline solution. According to the results, La@TG's addition to the epoxy coating greatly increased coating resistance because of its enhanced barrier qualities and active inhibition. The enhanced anti-corrosion performance of the La@TG coating can largely be attributed to the strengthened interactions at the coating-metal interface, as evidenced by increased adhesion strength in pull-off tests. Moreover, DMTA analysis indicated that incorporating the hybrid into the coating enhanced its thermal-mechanical properties, likely due to the synergistic effect between the inorganic component (lanthanum), which provides high mechanical stiffness, and the organic compounds, which offer flexibility and toughness. In summary, considering the significant improvement in corrosion protection and mechanical properties, La@TG is a promising candidate as an anti-corrosive pigment.

## Data availability

The original raw data is provided in the Supplementary Material.

Received: 5 March 2025; Accepted: 14 July 2025

Published online: 17 July 2025

## References

- Javidparvar, A. A., Farhadian, A. & Shahmoradi, A. R. Grafted cellulose as sustainable corrosion inhibitors, grafted biopolymers as corrosion inhibitors: safety, sustainability, and efficiency 337–363. (2023).
- Li, H. et al. Cutting fluid corrosion inhibitors from inorganic to organic: progress and applications. *Korean J. Chem. Eng.* **39** (5), 1107–1134 (2022).
- Abdallah, M., Jahdaly, B., Salem, M., Fawzy, A. & Fattah, A. A. Pitting corrosion of nickel alloys and stainless steel in chloride solutions and its Inhibition using some inorganic compounds. *J. Mater. Environ. Sci.* **8** (7), 2599–2607 (2017).
- Hansson, C. M. The impact of corrosion on society. *Metall. Mater. Trans. A*, 2952–2962 (2011).
- Funke, W. Problems and progress in organic coatings science and technology. *Prog. Org. Coat.* **31** (1–2), 5–9 (1997).
- Wang, J. et al. Long-term corrosion inhibition for AA5052 aluminum alloy by an eco-friendly hybrid inhibitor: synergism inhibition between Rosemary extract and zinc chloride in 0.05 M NaCl solution. *J. Ind. Eng. Chem.* **120**, 302–315 (2023).
- Wamba-Tchio, O. R. et al. Electrochemical study and experimental simulation of the synergistic effect of a formulation based on *Ficus pumila* linn. Leaves extract and zinc sulfate on the XC38 steel corrosion inhibition in NaCl solution. *J. Electroanal. Chem.* **919**, 116553 (2022).
- Qian, Y., Wu, Y., Guo, X. & Wang, L. A synergistic anti-corrosion effect of Longan residue extract and sodium dodecylbenzenesulfonate composition on AZ91D magnesium alloy in NaCl solution, corrosion engineering. *Sci. Technol.* **57** (4), 322–330 (2022).
- Zhu, C. et al. Synergistic effect between glutamic acid and rare Earth cerium (III) as corrosion inhibitors on AA5052 aluminum alloy in neutral chloride medium. *Ionics* **25**, 1395–1406 (2019).
- Sanaei, Z., Shahrabi, T. & Ramezanzadeh, B. Synthesis and characterization of an effective green corrosion inhibitive hybrid pigment based on zinc acetate-Cichorium intybus L. leaves extract (ZnA-CIL. L): electrochemical investigations on the synergistic corrosion inhibition of mild steel in aqueous chloride solutions. *Dyes Pigm.* **139**, 218–232 (2017).
- Ralkhal, S., Shahrabi, T. & Ramezanzadeh, B. Synthesis and construction of a highly potent hybrid organic/inorganic anti-corrosive pigment for effective corrosion control of mild steel in simulated seawater. *Constr. Build. Mater.* **222**, 400–413 (2019).
- Bahlakeh, G., Dehghani, A., Ramezanzadeh, B. & Ramezanzadeh, M. Combined molecular simulation, DFT computation and electrochemical studies of the mild steel corrosion protection against NaCl solution using aqueous Eucalyptus leaves extract molecules linked with zinc ions. *J. Mol. Liq.* **294**, 111550 (2019).
- Ramezanzadeh, M., Sanaei, Z., Bahlakeh, G. & Ramezanzadeh, B. Highly effective inhibition of mild steel corrosion in 3.5% NaCl solution by green nettle leaves extract and synergistic effect of eco-friendly cerium nitrate additive: experimental, MD simulation and QM investigations. *J. Mol. Liq.* **256**, 67–83 (2018).
- Koch, G. Cost of corrosion, Trends in oil and gas corrosion research and technologies 3–30. (2017).
- Revie, R. W. Corrosion and corrosion control: an introduction to corrosion science and engineering, John Wiley & Sons (2008).
- Basha, S. I. et al. Preparation of submicron-/nano-carbon from heavy fuel oil Ash and its corrosion resistance performance as composite epoxy coating. *J. Clean. Prod.* **319**, 128735 (2021).
- Kalendova, A., Veselý, D. & Kalenda, P. A study of the effects of pigments and fillers on the properties of anticorrosive paints. *Pigm. Resin Technol.* **35** (2), 83–94 (2006).
- Gao, X., Yan, R., Lv, Y., Ma, H. & Ma, H. In situ pretreatment and self-healing smart anti-corrosion coating prepared through eco-friendly water-base epoxy resin combined with non-toxic chelating agents decorated biomass porous carbon. *J. Clean. Prod.* **266**, 121920 (2020).
- Zoghalmi, A. & Zouaghi, M. Morphological variation in *Astragalus hamosus* L. and *Coronilla scorpioides* L. populations of Tunisia. *Euphytica* **134**, 137–147 (2003).
- Amin, G. Popular medicinal plants of Iran, Ministry of health 40–47. (1991).
- IUCN ([www.iucnredlist.org](http://www.iucnredlist.org)), *Trigonella grandiflora*, 2010.
- Schinella, G., Tournier, H., Prieto, J., De Buschiazio, P. M. & Rios, J. Antioxidant activity of anti-inflammatory plant extracts. *Life Sci.* **70** (9), 1023–1033 (2002).
- Ill-Min, C. et al. INHIBITION OF MILD STEEL CORROSION USING MAGNOLIA KOBUS EXTRACT IN SULPHURIC ACID MEDIUM, (2020).
- Muthukrishnan, P., Prakash, P., Jeyaprabha, B. & Shankar, K. Stigmasterol extracted from *Ficus hispida* leaves as a green inhibitor for the mild steel corrosion in 1 M HCl solution. *Arab. J. Chem.* **12** (8), 3345–3356 (2019).
- Muthukrishnan, P., Jeyaprabha, B. & Prakash, P. Mild steel corrosion inhibition by aqueous extract of *Hyptis suaveolens* leaves. *Int. J. Industrial Chem.* **5**, 1–11 (2014).
- Prabakaran, M., Kim, S. H., Kalaiselvi, K., Hemapriya, V. & Chung, I. M. Highly efficient *Ligularia fischeri* green extract for the protection against corrosion of mild steel in acidic medium: electrochemical and spectroscopic investigations. *J. Taiwan Inst. Chem. Eng.* **59**, 553–562 (2016).
- Cardó, X., Salagre, P. & Cesteros, Y. Layered double hydroxides for the catalytic isomerization of Linoleic acid to conjugated Linoleic acids (CLAs). *ChemEngineering* **3** (1), 30 (2019).
- Yousaf, A. B., Imran, M., Farooq, M. & Kasak, P. Interfacial phenomenon and nanostructural enhancements in palladium loaded lanthanum hydroxide nanorods for heterogeneous catalytic applications. *Sci. Rep.* **8** (1), 4354 (2018).
- Milanović, Ž. B. et al. Synthesis and comprehensive spectroscopic (X-ray, NMR, FTIR, UV–Vis), quantum chemical and molecular Docking investigation of 3-acetyl-4-hydroxy-2-oxo-2H-chromen-7-yl acetate. *J. Mol. Struct.* **1225**, 129256 (2021).
- Anand, K. et al. Degradation treatment of 4-Nitrophenol by *Moringa oleifera* synthesised GO-CeO<sub>2</sub> nanoparticles as catalyst. *J. Inorg. Organomet. Polym. Mater.* **28**, 2241–2248 (2018).
- Lite, M. C. et al. Design of green silver nanoparticles based on *Primula officinalis* extract for textile preservation. *Materials* **15** (21), 7695 (2022).
- Perrin, D. D. Dissociation constants of organic bases in aqueous solution: supplement 1972, Pergamon 1972.
- Xu, J. et al. Preparation and characterization of polyfluoroaniline/organosiloxane hybrid films. *J. Solgel Sci. Technol.* **69**, 580–585 (2014).
- Cihaner, A. & Önal, A. M. Synthesis and characterization of fluorine-substituted polyanilines. *Eur. Polymer J.* **37** (9), 1767–1772 (2001).
- Yu, Q. et al. Effects of fluorine atoms on structure and surface properties of PANI and fluorinated PANI/GPTMS hybrid films. *J. Solgel Sci. Technol.* **75**, 74–81 (2015).
- Saleem, S., Ahmed, B., Khan, M. S., Al-Shaeri, M. & Musarrat, J. Inhibition of growth and biofilm formation of clinical bacterial isolates by NiO nanoparticles synthesized from *Eucalyptus globulus* plants. *Microb. Pathog.* **111**, 375–387 (2017).
- Kumar, K. M., Hemanathan, E., Devi, P. R., Kumar, S. V. & Hariharan, R. Biogenic synthesis, characterization and biological activity of lanthanum nanoparticles. *Mater. Today: Proc.* **21**, 887–895 (2020).
- Ito, Y. Grazing-incidence small-angle x-ray scattering technique for nanostructure determination of surfaces and interfaces of thin films. *Rigaku J.* **25**, 1–6 (2009).
- Uchida, K., Mita, K., Higaki, Y., Kojio, K. & Takahara, A. Lamellar orientation in isotactic polypropylene thin films: a complement study via grazing incidence X-ray diffraction and surface/cross-sectional imaging. *Polym. J.* **51** (2), 183–188 (2019).



40. Adi, W., Taryana, Y. & Muzaki, R. Synthesis and characterization of composite UPR/Fe<sub>3</sub>O<sub>4</sub> for its use as electromagnetic wave absorber, IOP Conference Series: Materials Science and Engineering, IOP Publishing, p. 012033. (2017).
41. Chen, Z. Synthesis of monodisperse organic-and water-soluble iron oxide nanoparticles using Fe (OH) 3 as precursor. *J. Exp. Nanosci.* **9** (4), 406–414 (2014).
42. Joya, M., Barón-Jaimez, J. & Barba-Ortega, J. Preparation and characterization of Fe<sub>2</sub>O<sub>3</sub> nanoparticles, Journal of Physics: Conference Series, IOP Publishing, p. 012004. (2013).
43. Lu, J. & Tsai, C. J. Hydrothermal phase transformation of hematite to magnetite. *Nanoscale Res. Lett.* **9**, 1–8 (2014).
44. Ismail, W., Belal, A., Abdo, W. & El-Shaer, A. Investigating the physical and electrical properties of La<sub>2</sub>O<sub>3</sub> via annealing of La (OH) 3. *Sci. Rep.* **14** (1), 7716 (2024).
45. Ferby, V. A., Raj, A. M. E. & Bououdina, M. Structure and morphology of synthesized lanthanum hydroxide [La (OH) 3] nanocrystalline powders: study on fuel to oxidant ratio. *J. Aust. Ceram. Soc.* **56**, 711–720 (2020).
46. Smith, E. & Dent, G. *Modern Raman Spectroscopy: a Practical Approach* (Wiley, 2019).
47. Angel, S. M., Gomer, N. R., Sharma, S. K. & McKay, C. Remote Raman spectroscopy for planetary exploration: a review. *Appl. Spectrosc.* **66** (2), 137–150 (2012).
48. Bahlakeh, G., Ramezanzadeh, M. & Ramezanzadeh, B. Experimental and theoretical studies of the synergistic Inhibition effects between the plant leaves extract (PLE) and zinc salt (ZS) in corrosion control of carbon steel in chloride solution. *J. Mol. Liq.* **248**, 854–870 (2017).
49. Salehi, E., Naderi, R. & Ramezanzadeh, B. Synthesis and characterization of an effective organic/inorganic hybrid green corrosion inhibitive complex based on zinc acetate/urtica dioica. *Appl. Surf. Sci.* **396**, 1499–1514 (2017).
50. Kaghazchi, L., Naderi, R. & Ramezanzadeh, B. Synergistic mild steel corrosion mitigation in sodium chloride-containing solution utilizing various mixtures of phytic acid molecules and Zn<sup>2+</sup> ions. *J. Mol. Liq.* **323**, 114589 (2021).
51. Riazaty, P., Naderi, R. & Ramezanzadeh, B. Synergistic corrosion Inhibition effects of benzimidazole-samarium (III) molecules on the steel corrosion prevention in simulated seawater. *J. Mol. Liq.* **296**, 111801 (2019).
52. Santos, A. et al. Evaluation of palm kernel cake powder (Elaeis guineensis Jacq.) as corrosion inhibitor for carbon steel in acidic media. *Met. Mater. Int.* **27**, 1519–1530 (2021).
53. Frankel, G. S. & Landolt, D. Kinetics of electrolytic corrosion reactions. *Encyclopedia Electrochemistry: Online* (2007).
54. Yeganeh, M. & Keyvani, A. The effect of mesoporous silica nanocontainers incorporation on the corrosion behavior of scratched polymer coatings. *Prog. Org. Coat.* **90**, 296–303 (2016).
55. Liu, X. et al. Preparation and characterization of polyelectrolyte-modified attapulgite as nanocontainers for protection of carbon steel. *J. Electrochem. Soc.* **165** (13), C907 (2018).
56. Rahimi, A. et al. Bio-based and self-catalyzed waterborne polyurethanes as efficient corrosion inhibitors for sour oilfield environment. *J. Ind. Eng. Chem.* **123**, 170–186 (2023).
57. Zhong, F. et al. One-step hydrothermal synthesis of reduced graphene oxide/aspartic acid intercalated layered double hydroxide for enhancing barrier and self-healing properties of epoxy coating. *Reactive Funct. Polym.* **145**, 104380 (2019).
58. Mahdavian, M. & Attar, M. Another approach in analysis of paint coatings with EIS measurement: phase angle at high frequencies. *Corros. Sci.* **48** (12), 4152–4157 (2006).
59. Nguyen, T. & Martin, J. W. Modes and mechanisms for the degradation of fusion-bonded epoxy-coated steel in a marine concrete environment. *JCT Res.* **1**, 81–92 (2004).
60. Javidparvar, A. A., Naderi, R. & Ramezanzadeh, B. Epoxy-polyamide nanocomposite coating with graphene oxide as cerium nanocontainer generating effective dual active/barrier corrosion protection. *Compos. Part. B: Eng.* **172**, 363–375 (2019).
61. Mirzakhazadeh, Z. et al. Enhanced corrosion protection of mild steel by the synergetic effect of zinc aluminum polyphosphate and 2-mercaptobenzimidazole inhibitors incorporated in epoxy-polyamide coatings. *Corros. Sci.* **138**, 372–379 (2018).
62. Peng, Y. et al. Dual function of rare Earth carboxylate compounds on the barrier properties and active corrosion Inhibition of epoxy coatings on mild steel. *Prog. Org. Coat.* **185**, 107870 (2023).
63. Shahmoradi, A. R., Bejandi, M. S., Rasanani, E. H., Javidparvar, A. A. & Ramezanzadeh, B. Graphene oxide nano-layers functionalized/reduced by L-Citrulline/Pectin bio-molecules for epoxy nanocomposite coating mechanical properties reinforcement. *Prog. Org. Coat.* **178**, 107493 (2023).
64. Xian, G. & Karbhari, V. M. DMTA based investigation of hygrothermal ageing of an epoxy system used in rehabilitation. *J. Appl. Polym. Sci.* **104** (2), 1084–1094 (2007).
65. Levita, G., De Petris, S., Marchetti, A. & Lazzeri, A. Crosslink density and fracture toughness of epoxy resins. *J. Mater. Sci.* **26**, 2348–2352 (1991).
66. Penzien, J. et al. Generation and characterization of well-defined Zn<sup>2+</sup> + Lewis acid sites in ion exchanged zeolite BEA. *J. Phys. Chem. B.* **108** (13), 4116–4126 (2004).
67. Tang, H., Li, W., Zhou, H. & Cheng, X. One-pot synthesis of carbon fiber/carbon nanotube hybrid using lanthanum (III) chloride for tensile property enhancement of epoxy composites. *Appl. Surf. Sci.* **571**, 151319 (2022).
68. Javidparvar, A. A., Naderi, R. & Ramezanzadeh, B. Non-covalently surface modification of graphene oxide nanosheets and its role in the enhancement of the epoxy-based coatings physical properties. *Colloids Surf., A.* **602**, 125061 (2020).
69. Zhang, X., Nguyen, H., Daly, M., Nguyen, S. T. & Espinosa, H. D. Nanoscale toughening of ultrathin graphene oxide-polymer composites: mechanochemical insights into hydrogen-bonding/van der Waals interactions, polymer chain alignment, and steric parameters. *Nanoscale* **11** (25), 12305–12316 (2019).

## Author contributions

Mohammad Mahdavian and Mohammad-Bagher Gholivand conceived the idea and supervised the project. Mahya Olfatmiri ran the experiments and wrote the first draft of the manuscript. Mohammad Mahdavian and Mohammad-Bagher Gholivand edited the final version of the manuscript.

## Declarations

## Competing interests

The authors declare no competing interests.

## Additional information

**Supplementary Information** The online version contains supplementary material available at <https://doi.org/10.1038/s41598-025-11828-8>.

**Correspondence** and requests for materials should be addressed to M.-B.G. or M.M.

**Reprints and permissions information** is available at [www.nature.com/reprints](http://www.nature.com/reprints).

**Publisher's note** Springer Nature remains neutral with regard to jurisdictional claims in published maps and institutional affiliations.

**Open Access** This article is licensed under a Creative Commons Attribution-NonCommercial-NoDerivatives 4.0 International License, which permits any non-commercial use, sharing, distribution and reproduction in any medium or format, as long as you give appropriate credit to the original author(s) and the source, provide a link to the Creative Commons licence, and indicate if you modified the licensed material. You do not have permission under this licence to share adapted material derived from this article or parts of it. The images or other third party material in this article are included in the article's Creative Commons licence, unless indicated otherwise in a credit line to the material. If material is not included in the article's Creative Commons licence and your intended use is not permitted by statutory regulation or exceeds the permitted use, you will need to obtain permission directly from the copyright holder. To view a copy of this licence, visit <http://creativecommons.org/licenses/by-nc-nd/4.0/>.

© The Author(s) 2025